Distinct nanoscale membrane organizations of mucins and *trans*-sialidases in *Trypanosoma cruzi*

Gonzalo Escalante[1], Raquel Parada-Puig[2#], Lucía F. Lopez[1#], Alan M. Szalai[1#], María de los Milagros Cámara[2], Luciano A. Masullo[1§], Oscar Campetella[2], Juan Mucci*[2], Fernando D. Stefani*[1,3]

[1] Centro de Investigaciones en Bionanociencias (CIBION), Consejo Nacional de Investigaciones Científicas y Técnicas (CONICET), Godoy Cruz 2390, C1425FQD Ciudad Autónoma de Buenos Aires, Argentina.

[2] Instituto de Investigaciones Biotecnológicas (IIBio), Escuela de Bio y Nanotecnologías (EByN), Universidad Nacional de San Martín (UNSAM), Consejo Nacional de Investigaciones Científicas y Técnicas (CONICET), Av. 25 de Mayo y Francia, B1650HMP Buenos Aires, Argentina.

[3] Departamento de Física, Facultad de Ciencias Exactas y Naturales, Universidad de Buenos Aires, Güiraldes 2620, C1428EHA Ciudad Autónoma de Buenos Aires, Argentina.

[§]Present address: Max Planck Institute of Biochemistry, Am Klopferspitz 18, 82152 Planegg, Germany

Corresponding Authors:

* E-mail: fernando.stefani@df.uba.ar (FDS), jmucci@unsam.edu.ar (JM).

# These authors contributed equally to this work.

Keywords: Super-resolution microscopy, chagas disease, cell surface nanoscale organization

---

Abstract

Trypanosoma cruzi, the causative agent of Chagas disease, relies on surface sialylation to evade host immunity and invade cells. This process is mediated by *trans*-sialidases (TS) and mucins—an enzyme–substrate pair anchored to distinct lipid environments—yet how these molecules are organized at the nanoscale has remained unknown. Using dual-color super-resolution microscopy, we show that ~60% of mucins and TS are segregated into nanoclusters (~100 nm) that rarely contact each other, indicating that these abundant domains are unlikely to serve as primary sites of sialylation. In contrast, the ~40% fraction of non-clustered mucins and TS exhibit significantly shorter than random separation distances, consistent with organization on a shared fibrillar network. This architecture positions

non-clustered molecules within proximity compatible with catalytic activity, revealing a previously unrecognized spatial pathway for sialylation. Together, these findings uncover fundamental principles of *T. cruzi* surface organization with important implications for the regulation of host–parasite interactions.

Introduction

The parasite *Trypanosoma cruzi* (*T. cruzi*), the etiologic agent of Chagas disease or American trypanosomiasis, presents an unique mechanism to evade the host immune response that has intrigued researchers all over the world[1]. By covering its membrane with a dense coat of glycoproteins containing sialic acids, the parasite avoids lysis by serum factors[2,3] and achieves host-cell invasion[4]. Remarkably, *T. cruzi* is unable to synthesize sialic acids. Instead, it is part of a restricted group of parasites evolutionarily adapted to scavenge sialic acid from exogenous sialoglycoconjugates by means of a modified α(2–3)-sialidase known as trans-sialidase (TS), a GPI (Glycosylphosphatidylinositol)-anchored protein present on the cell surface of trypomastigotes[5]. In the presence of glycans with an α(2–3)-sialyl residue linked to a terminal β-galactose, the parasite's surface becomes rapidly sialylated through a glycosyl-transfer reaction driven by TS[6]. Although probably not the only acceptors available, mucins are considered the main targets for TS-transferred sialyl residues[2,7,8]. Mucins, with typical sizes ranging from 60 to 200 kDa, are a group of surface proteins, also GPI-anchored, that feature multiple *O*-linked oligosaccharide chains and are highly immunogenic[9].

The genome of *T. cruzi* encodes approximately 1,400 gene members of the TS-like superfamily[10] and 500 to 700 genes of the mucin family[11]. This diversity is key for the parasite's virulence by enhancing its capacity to modify its surface and evade host immune defenses[12,13]. Mucins and TS present distinct tertiary structures: the core of TS is typical of a globular glycoprotein, while mucins are highly O-glycosylated stick proteins[13].

Prior research revealed that TS and sialylated mucins, despite both being GPI-anchored, appear in separated membrane domains of *T. cruzi* trypomastigotes[14]. The discovery of the segregated distribution of mucins and TS raised significant questions regarding the mechanisms that regulate their compartmentalization and interaction[14]. However, the limited spatial resolution of those early studies did not allow a detailed characterization of either the size or the spatial organization of the mucins and TS domains.

It has also been determined that mucins and TS membrane domains exhibit distinct biochemical organizations, with mucin domains possessing lipid raft characteristics, while TS domains lack them[14,15]. Notably, this correlates with the fact that, in the mammalian stage of

the blood trypomastigote, these proteins associate to different lipids: mucins are bound to alkyl-acylglycerol and TS contains ceramide[16,17]. While in mammalian cells ceramide has not been found in GPI-anchored proteins, alkyl-acylglycerol (and diacylglycerol to a lesser degree) is a key determinant of their association with lipid rafts[18,19]. Therefore, this unique lipid composition could explain the differential membrane organization.

Here, we apply two-color super-resolution fluorescence microscopy combined with clustering analysis, molecular distance quantification, and model-based simulations to resolve the nanoscale landscape of TS and sialylated mucins on the surface of *T. cruzi* trypomastigotes with unprecedented detail. This integrated approach allows us to test whether the long-standing view of mucin–TS interactions—largely inferred from biochemical assays and diffraction-limited imaging—holds true at the nanometer scale where catalysis occurs. By directly quantifying cluster sizes, spatial distributions, molecular proximities, and the underlying structural dimensionality, we uncover architectural principles that reshape our understanding of how these key virulence factors are organized and potentially coordinated on the parasite membrane. Ultimately, this framework enables us to propose a spatially grounded hypothesis for where functional sialylation can occur *in vivo*, providing a foundation for future mechanistic studies of host–parasite interactions.

Results

Nanoscale distribution of mucin and trans-sialidase domains

We applied two-color Stochastic Optical Reconstruction Microscopy (STORM)[20,21] on fixed *T. cruzi* parasites in the infective trypomastigote form. The SAPA region of TS–the C-terminal domain composed primarily of immunodominant amino acid repeat units[22]–was immunoconjugated with Alexa Fluor 568. Sialylated mucins were labeled with Alexa Fluor 647. To label sialylated mucins, we followed an unnatural sugar approach that enables labeling TS target proteins with higher selectivity and minimal background compared to the use of mucin-directed antibodies or lectins[6,23].

Super-resolution imaging reveals that an important fraction of mucins and TS are organized into separated nanometric domains (Figure 1A). By contrast, conventional diffraction-limited microscopy only provides rough signs of segregation for these two proteins (Figure 1B), as previously reported[14].

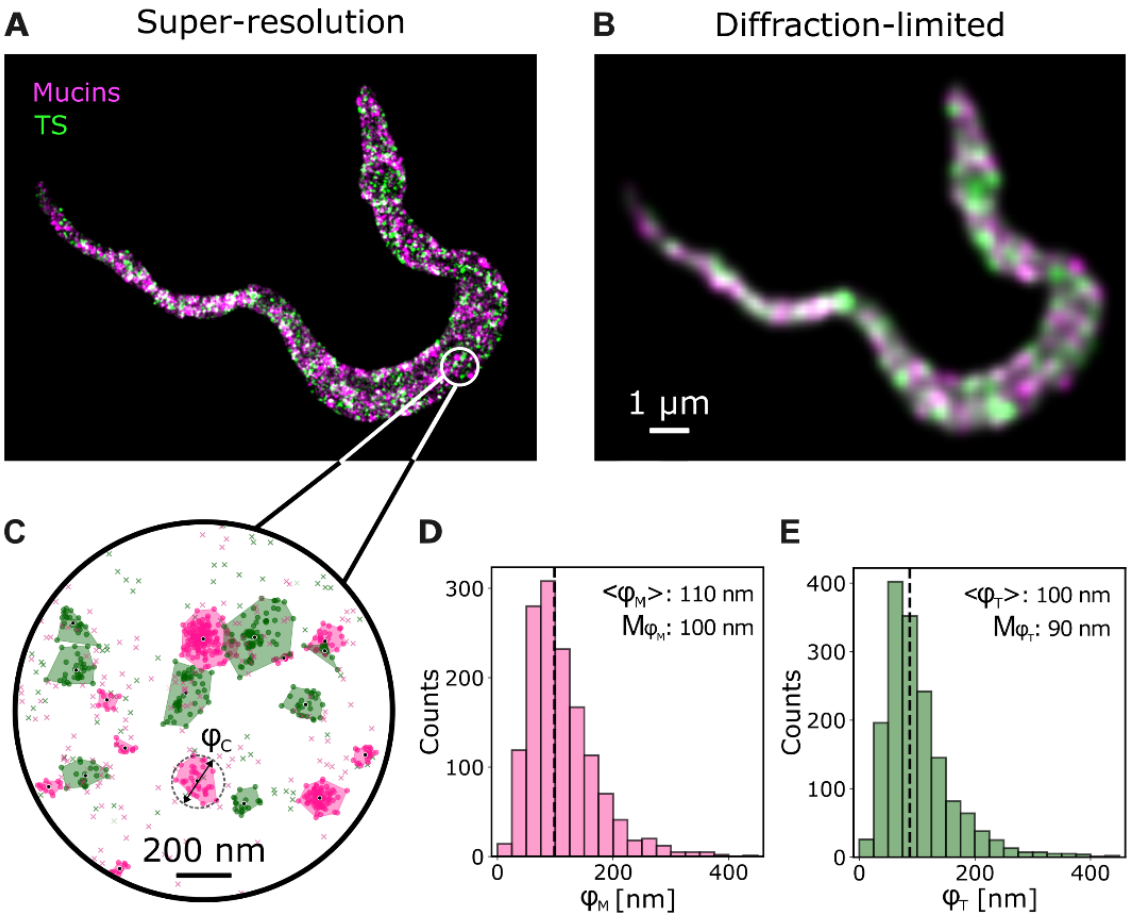

Figure 1. Mucins and TS in *T. cruzi* plasma membrane. (A) Two-color super-resolution (STORM) image based on single molecule localizations of mucins (magenta) and TS (green) in a *T. cruzi* trypomastigote. **(B)** Two-color diffraction-limited fluorescence image of the same parasite. **(C)** Zoom-in of a membrane region showing the localizations of mucins and TS. Localizations classified as clustered using DBSCAN are represented with dots while non-clustered localizations are represented with crosses. The estimation of the effective diameter of the clusters (φ_C) is depicted. **(D, E)** Distributions of effective cluster diameters of mucins (**D**, φ_M) and TS (**E**, φ_T). The average effective diameters are indicated in brackets, while the medians are marked with dotted lines and represented as Mφ.

To analyze the spatial distribution of the molecular localizations, we employed a density-based clustering algorithm (DBSCAN)[24] and a density-based clustering validation[25] to detect clusters of mucins and TS from the STORM data. Overall, 184 membrane areas were analyzed from 25 trypomastigotes. 1617 clusters of TS and 1413 clusters of sialylated mucins were identified, with heterogeneous sizes and shapes. The cluster size was quantified as the diameter of the smallest circle including the cluster (Figure 1C). The histograms of cluster size reveal monomodal, positively skewed distributions with mean

values of 110 and 100 nm for mucins and TS, respectively (Figures 1D and 1E). The median cluster diameters for mucins and TS were determined to be 100 nm and 90 nm, respectively, in agreement with previous results using single-color GSDIM super-resolution microscopy[14]. These sizes are well below the diffraction limit and are comparable to the sizes of other reported membrane protein clusters, such as T-cell receptors (from 70 nm to 140 nm)[26] and to reported lipid rafts sizes (up to 200 nm)[27].

Several studies have established that crosslinking agents can potentially generate or stabilize protein clusters[28–31]. In our previous work, where the membrane segregation of mucins and trans-sialidases was first detected[14], numerous fixation reagents and temperatures were tested in order to confirm the biological origin of the observed protein organization. Moreover, a rapid membrane fluidization using diethyl-ether abolished the distinct pattern observed[14]. Here, we further confirm that the observed nanodomains are not produced by the fixation protocol by observing a uniform distribution of the highly abundant Variant Surface Glycoprotein (VSG) in *Trypanosoma brucei* using the same fixation protocol as in our measurements of mucins and TS in *T. cruzi* tissue-culture derived trypomastigotes (Supplementary Figure 1). Moreover, we also note that the maximal reported size of fixation-induced protein clusters after PFA, GA, or MeOH was of 14–16 nm in diameter[30]. In contrast, the domains revealed in this work present mean effective diameters about an order of magnitude larger. In support of the aforementioned, the idea that fixation is not responsible for the observed spatial organization of mucins and TS.

Once these nanodomains were identified, a relevant question arises as to whether they are randomly distributed or if they follow any other underlying organization. To address this question, we calculated the distribution of nearest-neighbor distances between the centers of mass of the experimentally observed clusters of mucins (d_{MM}) and TS (d_{TT}), and compared those distributions to those obtained from the same clusters in randomized positions within the same observation areas (Figure 2A). One hundred random distributions were simulated for each one of the experimentally observed sets of clusters. The distributions and cumulative distribution functions (CDF) of d_{MM} and d_{TT} are shown in Figures 2B and 2C, respectively, for the experimentally observed and the randomized distributions of clusters. For the randomized distributions, all the individual CDFs are shown (grey) along with their average (black). Remarkably, neither mucins nor TS clusters follow a random distribution over the parasite membrane. The first neighbor distances between mucin clusters are larger than those of a random distribution, indicating that these clusters are segregated. By contrast, TS clusters are found at shorter distances compared to those expected in a random distribution. These observations, supported by a two-sample Kolmogorov-Smirnov test ($p = 1.4\times10^{-3}$ for d_{MM}; $p = 1.1\times10^{-9}$ for d_{TT}), indicate that the clusters of mucins and TS are not randomly distributed but reflect an underlying membrane organization.

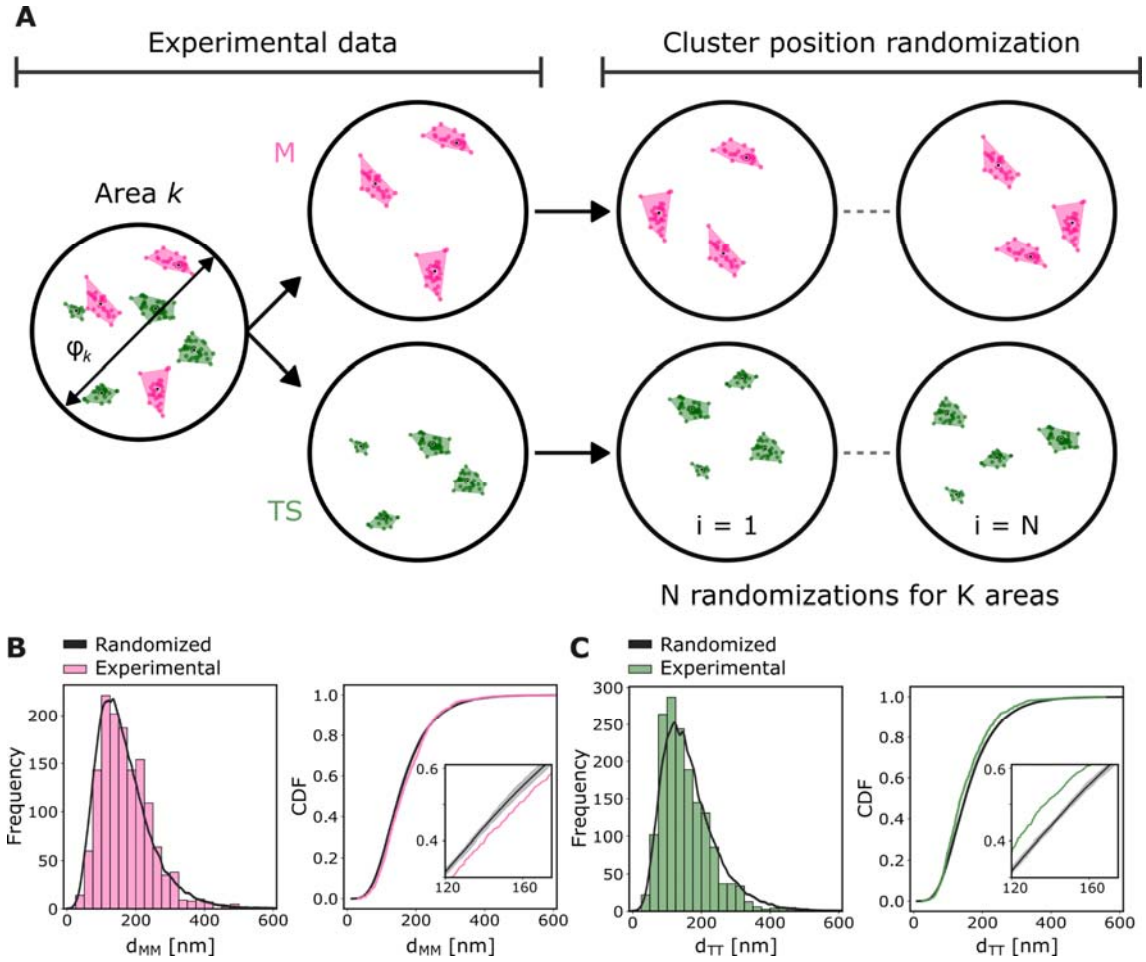

Figure 2. Characterization of the spatial distribution of mucins and TS nanodomains. (A) Schematic description of the cluster position randomization: within each experimentally observed area, the clusters found with DBSCAN were relocated in random positions ensuring that they do not overlap to avoid cluster merging. **(B,C)** Histogram and Cumulative Distribution Function (CDF) of first neighbor distances between the mass centers of experimental and randomized clusters of mucins (**B**, d_{MM}) and TS (**C**, d_{TT}). The CDFs of 100 randomized distributions are displayed in grey, with their average highlighted in black. A zoom-in is shown in the insets to better appreciate the differences between the curves.

Separation distances and overlap between mucins and TS domains

Next, we analyzed the nearest-neighbor cross distances and overlap between clusters of mucins and TS, and compared the experimentally observed parameters to those obtained from a random distribution of domains. In this case, in order to model random contacts realistically, the native, non-random arrangements of clustered mucins and TS had to be preserved. To achieve this, we shuffled the experimentally determined mucin clusters from one area with TS clusters from another area, maintaining their original organization (Figure

3A). The distribution of experimental first neighbor distances from mucin clusters to TS clusters (p = 0.06) and *vice versa* (p = 0.33) cannot be distinguished from a random scenario (Figures 3B and 3C).

To study the spatial overlap between domains of mucins and TS, a two-dimensional Gaussian rendering was applied to the localizations. The resulting rendered images were then converted into binary masks. The overlap areas were quantified by computing the overlapping pixels between the mucin and TS masks (Figure 3D). For this parameter as well, the experimental distributions did not differ significantly from a random model (Figure 3E; K-S statistic = 0.09, p = 0.09).

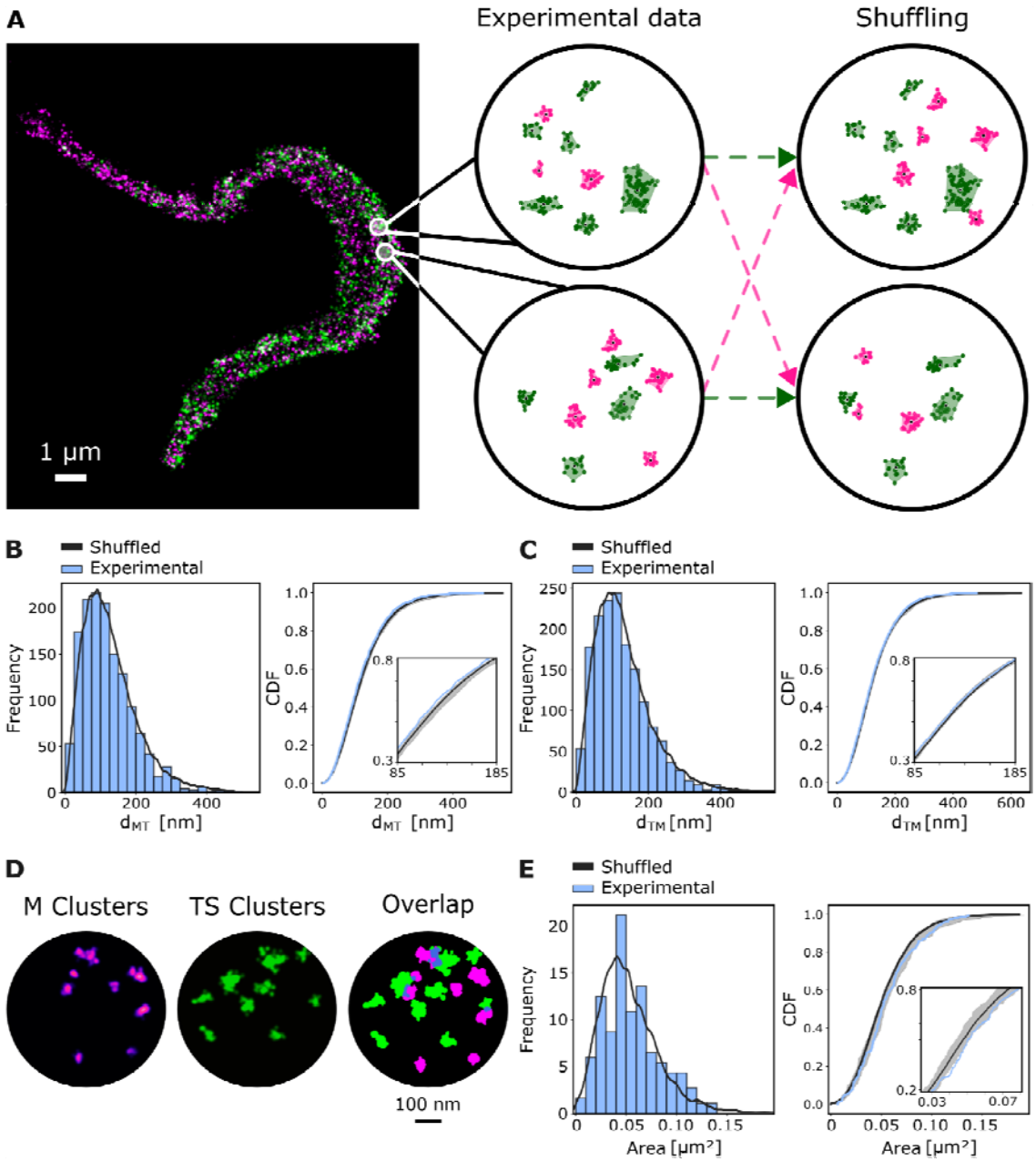

Figure 3. Separation distances and overlap between mucins and TS nanodomains. (A) Shuffling of experimental data: given two circular areas of equal diameter of *T. cruzi* membrane, mucin clusters from one area are combined with TS clusters from the other (and vice-versa). First neighbor distances from the mass centers of mucins clusters to TS clusters (d_{MT}) and vice versa (d_{TM}) are determined. **(B,C)** Histogram and CDF of first neighbor cross-distances (**B**, d_{MT} – **C**, d_{TM}). For each case, the CDFs of 100 randomized distributions are displayed in grey, with their average highlighted in black. **(D)** Example of 2D Gaussian rendering of an experimental cluster dataset: mucins clusters in magenta, TS clusters in green, overlap areas in blue. **(E)**. Histogram and CDF of overlap areas between mucins and TS clusters for experimental and shuffled data.

Spatial arrangement of non-clustered mucins and TS

Importantly, 38% of the mucins and 42% of the TS are located outside clusters. The distributions of first-neighbor distances between non-clustered mucins (M-M) or non-clustered TS (T-T) do not provide any insight into their molecular distributions because they both present a peak at the average localization precision (~10 nm) (Figure 4A), which is explained by multiple localizations of the same fluorophore (multiblinking)[32] and/or multiple labeling of the same protein. On the other hand, the cross-distance distributions, from mucins to TS (d_{MT}) and *vice versa* (d_{TM}), present broader distributions with larger mean values of 35 nm and 45 nm, respectively (Figure 4B).

The question then arises of whether these distributions are simply due to the varying abundance of each protein and random placement over the available space, or if they reflect some other underlying organization. We thus compared the experimental distributions to simulated random distributions, considering the same number of experimental localizations and the membrane area not occupied by clusters. In order to maintain the original distributions of non-clustered localizations of mucins and TS, we applied the same shuffling method used for the clusters. To implement this approach, we sampled the membrane not occupied by clusters with square regions, as shown in Figure 4C. We ensured that each square area contained both mucins and TS molecules. The size of the square region was chosen as the minimum that encloses the maximum first neighbor distances observed experimentally for d_{MT} and d_{TM} (~200 nm, Figure 4B), namely 146 nm x 146 nm with a diagonal of 206 nm. In this way, we maximize the area of non-clustered proteins analyzed while respecting the maximum first neighbor distances observed experimentally.

Figure 4D shows the distributions and CDFs of first neighbor cross distances for the native distribution of non-clustered mucins and TS molecules, and for the randomized (shuffled) localizations obtained from combining mucins from a given square sample area with TS from another one. In both cases (d_{MT} and d_{TM}), the shuffled localizations exhibit overall larger

distances, indicating that the non-clustered mucins and TS do not occupy the entire available membrane. Instead, they are confined to smaller compartments or structures that shorten the separation distances to their nearest counterpart.

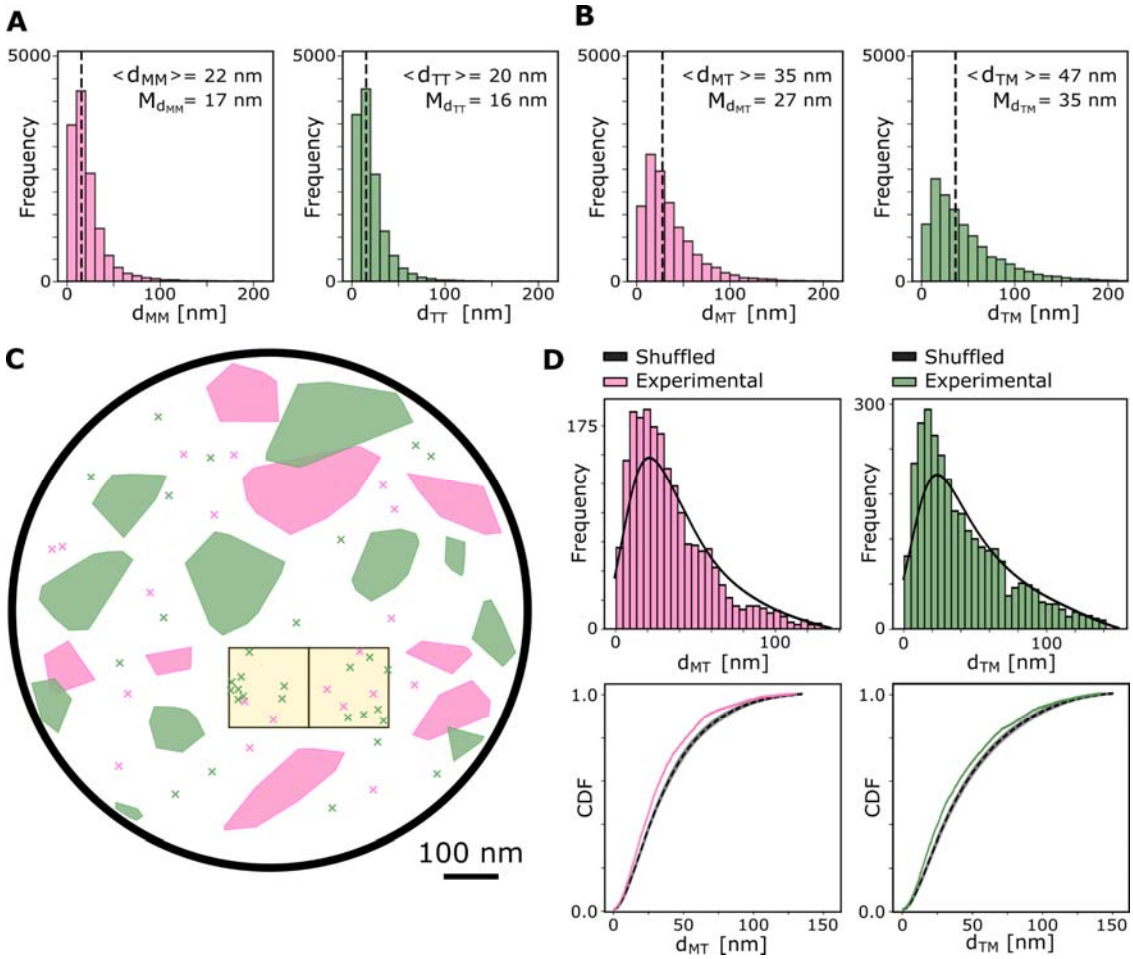

Figure 4. Analysis of the spatial distribution of non-clustered mucins and TS molecules. (A,B) Histograms of the first neighbor distances of non-clustered proteins of the same kind (**A**, d_{MM} and d_{TT}) and between mucins and TS (**B**, d_{MT} and d_{TM}). Mean values are reported in brackets and the median is shown as a dashed line. **(C)** Schematic of the sampling of the membrane left available by the clusters using square areas. In each one of the 184 circular areas analyzed, the membrane area not occupied by clusters was sampled by taking non-overlapping, non-repetitive squares with a side of 146 nm, ensuring that they contained both mucins and TS localizations. **(D)** Histogram and CDF of experimental d_{MT} (magenta) and d_{TM} (green) compared to the distance distributions obtained from shuffling mucins and TS localizations from different square areas (in black). Kolmogorov–Smirnov test p-values are 2.5×10^{-15} for d_{MT} and 3.9×10^{-14} for d_{TM}.

A way to gain insight into the spatial confinement of the non-clustered mucins and TS is by studying the dimensionality (*n*) of the underlying space in which these localizations reside[33]. This approach is based on examining the distance dependence of the complementary cumulative distribution function (CCDF) of the nearest-neighbor distance, and enables determining the basic organization of molecules even in highly sparse conditions[33]. Molecules randomly organized in one dimension (1D) present a value of $n = 1$. Molecules distributed randomly in 2D yield a value of $n = 2$. Distributions where molecules are organized in confined structures (e.g., crossing fibers) can attain values of *n* between 1 and 2 (Figure 5A)[33]. Performing this analysis on the localizations of non-clustered mucins and TS reveals that both proteins show the same average value of $n = 1.36$ (Figure 5B), confirming confinement and suggesting that they may share a common compartmentalization.

Using simulations, we tested three models of compartmentalization of the non-clustered mucins and TS: circular compartments, rectilinear fibers, and curved fibers. The simulations consisted of defining compartments within 146 nm x 146 nm squares, filling them with mucins and TS localizations at random positions so as to obtain an overall surface density equivalent to that observed experimentally, and computing *n*. In the case of the circular compartments the position, number and diameter of the compartments were varied. In the case of fibers, the number (N), position, orientation and width (w) of the fibers were varied (Figure 5C). It was not possible to reproduce the experimental dimensionality of $n = 1.36$ with the model of circular compartments, regardless of the compartment parameters used (Supplementary Figure 2A); this model led to values of n closer to the extreme values of 1 or 2, and was therefore ruled out. By contrast, both fibrillar models retrieved values of dimensionality comparable to the experiments ($n = 1.30$-1.42) for several combinations of $2 \leq N \leq 6$ and $10 \leq w \leq 20$. Figure 5D shows the results for the model of rectilinear fibers (see Supplementary Figures 2B and 2C for further results).

A more direct comparison to the experiments can be obtained by evaluating the CDFs of first neighbor cross distances of simulations where molecules were randomly distributed over a mesh of 4 rectilinear fibers of 10 nm width inside an area of 146 nm x 146 nm, while keeping the overall density of molecules equal to the experimentally observed one (further results for the curved fibers and linear fibers in Supplementary Figures 3 to 6). In this way, we generated variations of molecular distributions with a similar density and dimensionality (n) as the experimentally observed for mucins or TS. Then, we computed the CDF of first neighbor cross distances in two situations: distributing the simulated mucins and TS over the same fibers or over different fibrillar scaffolds (Figure 5D). The latter was achieved by shuffling mucin and TS positions from different simulations, just as was done with the experimental data from different regions. The nearest-neighbor cross-distance increased when mucins and TS were distributed in independent fibrillar meshes, just as observed when

the experimental data was shuffled for randomization. This result strongly suggests that the positions of both proteins are determined by the same underlying structure. Otherwise, if both proteins were already distributed in independent structures with a dimensionality of n = 1.36, shuffling their relative positions should not have an effect on their relative separation.

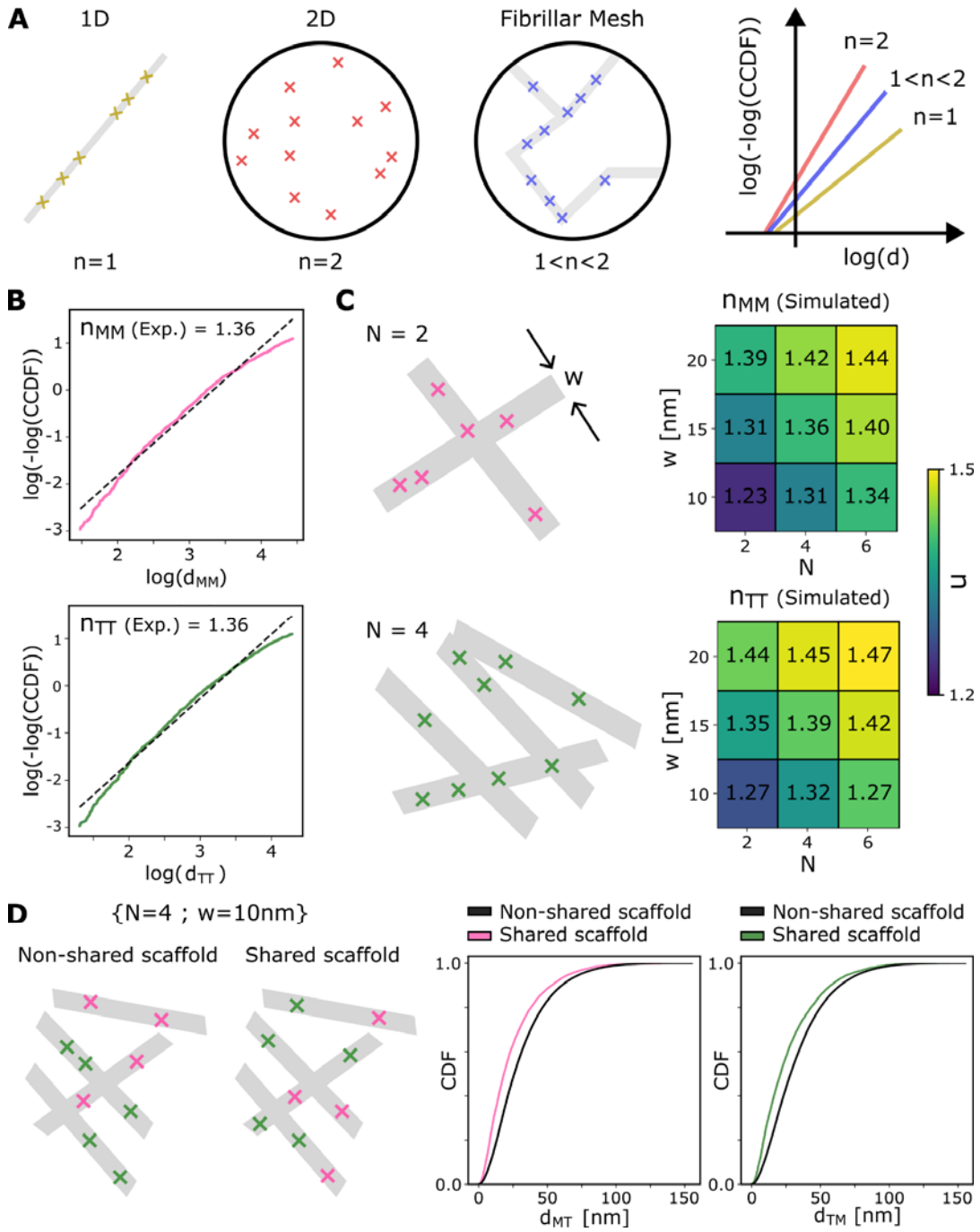

Figure 5. Dimensional analysis of non-clustered mucins and TS molecules. (A) Functional dependence of the complementary cumulative distribution function (CCDF) of the distance to the first

neighbor (d) for various point distributions. The log[-log(CCDF)] as a function of the log(d) is a linear function whose slope *n* (dimensionality) takes extreme values of 1 for a strictly linear arrangement (1D) and 2 for a random 2D distribution. Intermediate organizations such as a fibrillar networks present values of $1 < n < 2$. **(B)** log[-log(CCDF)] vs. the experimentally observed first neighbor distances of mucins (d_{MM}) and TS (d_{TT}). Dotted lines are linear fits retrieving a value of $n = 1.36$ in both cases. **(C)** Schematic of molecules distributed over a mesh of N rectilinear fibers of width (w). Average values of n obtained from simulations randomly distributing a density of molecules equal to the experimentally observed for mucins and TS over N (2, 4, or 6) rectilinear fibers of various thicknesses (10, 15 or 20 nm) inside an area of 146 nm x 146 nm. For each condition, 10,000 simulations were performed. Results for other combinations of N and thickness are presented in Supplementary Figures 2B and 2C. **(D)** Schematic representations illustrate two scenarios: mucins and TS arranged on separate fibrillar scaffolds versus both sharing a common scaffold. The plots show cumulative distribution functions (CDFs) of first-neighbor cross-distances derived from simulations. In these simulations, molecules were randomly distributed at densities matching experimental observations across a mesh of four rectilinear fibers (10 nm wide) within a 146 × 146 nm area. Magenta and green curves represent CDFs of distances from mucins to TS and TS to mucins, respectively, when both proteins share the same scaffold. The black curve corresponds to the scenario where mucins and TS occupy distinct fibrillar scaffolds.

Discussion

The structure and dynamics of the *Trypanosoma cruzi* membrane remain poorly understood. Our results provide new insights into the nanoscale spatial organization of mucins and *trans*-sialidases (TS) in trypomastigote membranes.

Spatial analysis of single-molecule localizations revealed two distinct configurations for mucins and TS. First, consistent with previous reports[14], a large fraction (~60%) of these proteins segregate into clusters. The higher resolution achieved in this study allowed us to determine their sub-diffraction sizes, averaging ~100 nm for both mucins and TS. Although mucins and TS clusters are similar in size, their distributions differ markedly. In comparison to a random distribution, mucin clusters are more widely spaced while TS clusters are more closely packed. Second, the remaining ~40% of molecules that are non-clustered exhibit mucin-TS separation distances closer than random, and a distribution consistent with organization along a common fibrillar mesh.

Previous studies proposed that the spatial separation of mucins and TS clusters could hinder efficient sialylation[13]. Our results support this interpretation. Given the ~50 nm catalytic reach of TS, we computed that only ~15% of mucin–TS cluster pairs fall within a range theoretically compatible with sialylation—and even then, only peripheral molecules would be accessible. Furthermore, the observed overlap between mucin and TS clusters is consistent

with random contacts, reinforcing the idea that clustered states are unlikely to be functional sites of sialylation.

Importantly, the 40% of non-clustered mucins and TS display a non-random distribution. Their nearest-neighbor distances are significantly shorter than expected by chance, and spatial confinement analysis (dimensionality n = 1.36) suggests organization along narrow fibers (10–15 nm wide). Cross-distance distributions (medians of 35 nm for mucin→TS and 47 nm for TS→mucin) indicate that over 60% of these non-clustered molecules lie within the theoretical catalytic range for sialylation. We emphasize that this interpretation of the spatial organization of mucins and TS does not constitute direct evidence of sialylation occurring in these regions. It constitutes a new hypothesis based on the findings of this study, which could serve as a guideline for future research. Functional assays on live infectious parasites are not trivial, but could provide definitive evidence to test this new hypothesis.

In conclusion, our work provides the first nanoscale map of mucins and trans-sialidases on the *T. cruzi* membrane, revealing two coexisting organizational modes with distinct functional implications. Approximately 60% of both proteins form segregated nanoclusters whose spatial separation makes catalytically meaningful interactions highly unlikely. In contrast, a substantial fraction of the remaining ~40% of non-clustered mucins and TS lie within distances compatible with efficient sialylation. Spatial analyses further indicate that these non-clustered molecules may be positioned by a shared underlying fibrillar network, suggesting coordinated organization rather than random dispersal.

Altogether, these findings support a new working model for possible sialylation at the parasite surface, occurring predominantly between the non-clustered, fibrillary-organized mucins and TS, rather than in the abundant clustered pools. Although functional assays in live parasites will be required to test this hypothesis directly, our results establish a quantitative framework for understanding how membrane architecture shapes parasite persistence and virulence. More broadly, this work highlights the power of nanoscale imaging to uncover organizational principles that are otherwise invisible yet central to the biology of protozoan pathogens.

Materials and Methods

Ethics statement

The protocol of animal immunization followed in this study was approved by the Committee on the Ethics of Animal Experiments of the Universidad Nacional de San Martín, according to the recommendations of the Guide for the Care and Use of Laboratory Animals of the National Institutes of Health.

Parasite cultures

T. cruzi CL Brenner tissue culture-derived trypomastigotes were obtained from infected Vero cells growing at 37°C and 5% CO_2 in minimum essential medium (MEM) supplemented with 4% (v/v) fetal bovine serum (FBS), 0.292 g/l L-glutamine, 100 IU/ml Penicillin and 100 µg/ml Streptomycin (all from Gibco, NY).

Sialic acid acceptor molecules labeling

Sialic acid acceptors on the surface of *T. cruzi* trypomastigotes were labeled via the Staudinger-Bertozzi click-chemistry approach, employing the trypomastigote endogenous TS[14]. Briefly, tissue culture-derived trypomastigotes were harvested by centrifugation, washed twice with Phosphate Buffered Saline (PBS, 137 mM NaCl, 2.7 mM KCl, 1.8 mM KH_2PO_4, 10mM Na_2HPO_4, pH 7.4; Gibco) and resuspended at a density of $1x10^6$ cells/µl. Parasites were then incubated in PBS with 1mM Neu5Az-GalβOMe (Neu5AzGal was synthesized following previously established methods[34]) and then washed with PBS. Afterwards, sialylated parasites were incubated with 50µg/ml of FLAG conjugated dibenzocyclooctyne (DBCO-$(PEG)_4$-FLAG, Jena Bioscience, Germany) for the click-chemistry reaction. Following two additional PBS washes, labeled parasites were fixed with 4% PFA in PBS. All three incubations were 30 min long and conducted at room temperature.

Immunostaining

Tissue-derived trypomastigotes – labeled as described above – as well as exponentially grown epimastigotes and *T. brucei* bloodstream trypomastigotes were collected by centrifugation and extensively washed with PBS. Parasites were then resuspended in PBS containing 4% (v/v) p-formaldehyde (PFA, Electron Microscopy Sciences, PA) and fixed for 30 min, followed by washing and resuspension in PBS. Fixed parasites were settled on poly-L-lysine-coated coverslips (16 or 22mm Φ; Marienfeld, Germany) for 1 h. Unattached cells were then removed by washing with PBS. Subsequently, samples were incubated 30 min in a blocking solution (BS) consisting of 0.45µm-filtered 5% (w/v) biotechnology grade-bovine serum albumin (BSA, Amresco, OH), 100mM NH_4Cl and 2.5% horse serum in PBS. Then, samples were probed with in-house-made antisera (mouse anti-SAPA, 1:3000 or rabbit anti-VSG-221, 1:2000) and/or rat anti-FLAG mAb M2 clone, 1:1000 (Sigma) diluted in BS. Following extensive washes with PBS, the corresponding Alexa Fluor-conjugated secondary antibodies (Invitrogen, IL) diluted in BS to a final concentration of 2µg/ml were added. Both primary and secondary antibody incubations were 1 h long and all steps were performed at room temperature in a humid chamber. DAPI (4',6-diamidine-2'-phenylindole dihydrochloride) was used (CalBiochem, Germany) to visualize the nucleus and kinetoplast before montage with FluorSave reagent (Merk).

For two-color STORM samples, post-labeling fixation was performed as described above in a 6-well polystyrene plate (Corning) and samples were stored in PBS at 4°C until processed. Alexa Fluor 568 and Alexa Fluor 647 were chosen due to the low crosstalk between their emission spectra and their performance for STORM imaging[32].

Imaging

The STORM microscope was custom-built around a commercial inverted microscope stand Olympus IX-73 operating in wide-field epifluorescence mode. A 642 nm 1.5 W laser (MPB Communications 2RU-VFL-P-1500–642) and a 532 nm 1.5 W laser (Laser Quantum Ventus 532), both circularly polarized, were used for fluorescence excitation. A 405 nm 50 mW diode laser (RGB Photonics Lambda Mini) was used for reactivating fluorescent molecules. The lasers were focused to the back focal plane of the oil immersion objective Olympus PlanApo 60x NA 1.42. Collected fluorescence light was decoupled from the laser excitation by a quad-edge multiband mirror (Semrock Di03-R405/488/532/635-t1). Further blocking of the illumination lasers was performed with a quad-notch filter NF (Semrock NF03-405/488/532/635E-25).

Dual-color simultaneous imaging was performed through emission wavelength discrimination. A dichroic lowpass filter (Chroma ZT647rdc) and two band-pass filters (Semrock 582/75 BrightLine HC and Chroma ET700/75m) were used to separate the fluorescence emission from Alexa Fluor 568 and Alexa Fluor 647, respectively.

Differences in magnification, shear and image rotation between the two channels were corrected prior to acquisition by imaging multicolor beads (Life Technologies Tetraspeck 0.1 µm), performing an affine transformation correction for the overlay of channels (Hartley & Zisserman, 2018). The emission light was expanded with a 2x telescope so that the pixel size of the EMCCD camera (Andor iXon3 897 DU-897D-CS0-#BV) was 133 nm in the sample plane. The camera and lasers were controlled with Tormenta, a custom software developed in the laboratory (Barabas et al., 2016).

STORM sample preparation

22 mm coverslips containing fixed parasites were placed in a holder and imaging was performed in STORM imaging buffer (50 mM Tris, 10 mM NaCl, 10% w/v glucose, pH=8) supplemented with 1 µg/ml glucose oxidase (Sigma-Aldrich), 0.5 ug/mL catalase (Sigma-Aldrich) and 10 mM MEA (mercaptoethylamine) as oxygen scavenging system.

Image acquisition

Prior to STORM imaging, conventional fluorescence images of the region of interest were acquired by setting the excitation laser power density to 1-3 W cm^{-2}. The channel overlay

calibration was performed before each measurement routine. Super-resolution data acquisition was then started by changing the excitation laser power density to 10-20 kW cm^{-2}, inducing on-off switching of the fluorophores. Given that the parasites are approximately 1 µm thick, the illumination was set up in epifluorescence mode. Throughout the whole acquisition, the 405 nm laser power was increased whenever the density of single-molecule blinking events decreased below 1 molecule per μm^2. Generally, it took 20000-25000 frames with an exposure time of 50 ms for each STORM acquisition.

Image post-processing

Picasso software[35] was employed for the detection and fitting of single-molecule events using the MLE Integrated Gaussian method[36]. Localizations were filtered based on the global estimated precision – 11 nm – obtained with the NeNA algorithm[37]. Picasso was also used for rendering super-resolution images. Additionally, redundant cross-correlation (RCC) drift correction was applied to all datasets (in each one, we first corrected the drift via RCC in one of the emission channels to generate a drift-correction file, which was then applied to correct the drift in the second channel to ensure that both channels had the exact same correction). For the subsequent analysis of data, 184 circular areas with variable known diameters were selected from 25 parasites - without overlapping - from the entire set of measured parasites. The selection was unbiased, ensuring that no specific region of the parasite's structure influenced the choice. Localizations within each selected area were then exported for further processing. The parasite edges were excluded to reduce artifacts caused by 2D axial projections.

Clustering analysis and simulations

The spatial distribution of mucins and TS was analyzed in a total of 25 parasites derived from three independent replicates. Specifically, the number of parasites analyzed from each replicate was 11, 6, and 8 parasites, respectively. DBSCAN[24] – Density-Based Spatial Clustering of Applications with Noise – was applied to the lists of STORM localizations obtained. This clustering method was chosen due to the unknown number and shape of the clusters and the presence of isolated localizations in the data (noise). The MinPoints parameter was set to 10, following the mean number of switching cycles expected for Alexa Fluor 568 and Alexa Fluor 647[32]. The density-based clustering validation (DBCV)[25] was employed for hyperparameter tuning, given that we lacked prior information about the features of the domains under study. The DBSCAN search radius (ε) was varied from 10 nm to 40 nm in 1 nm increments, and for each area, the combination of fixed MinPoints and the optimal ε value that yielded the highest validation index was selected.

For the randomization of the experimental clusters, the positions of their centers of mass were randomly relocated inside the selected circular area. This process involved initially loading the cluster data, including positions and mass centers. For each cluster, a random point within the area was generated, and the cluster was then shifted to this new position, ensuring it remained within the circle's boundary and did not overlap with previously relocated clusters. Overlaps were assessed by computing the convex hulls of the clusters and checking for intersections between them.

In the shuffling method applied to clustered localizations, a mucin dataset from an area was combined with a TS dataset from another area, ensuring that the diameters of the selected areas were the same. This approach was used to study cross metrics, as it was not possible to replicate them through simulations due to the segregated/almost random nature of mucins among themselves and the anti-segregated nature of TS. To quantify the overlap between clusters and estimate their area of occupancy, we generated an image by rendering each localization with a normalized Gaussian. For each normalized Gaussian, we used a standard deviation of 10 nm (i.e., the localization precision). The pixel size of the rendered images was 5 nm. These images were then thresholded using the standard deviation of the rendered image to create binary masks (σ = 10 nm). The overlap between the masks was determined by counting the number of overlapping pixels. The total occupied areas for the mucin and TS masks were similarly calculated by summing the pixels in each mask. Finally, occupancy percentages were computed as the ratio between occupied areas and the total area.

Dimensional analysis and fibers simulations

To assess the spatial organization of molecular localizations, we analyzed the functional dependence of the complementary cumulative distribution function (CCDF) of the first neighbor distance (r_1)[33]. This method exploits the scaling behavior of the number of molecules encountered within a given radius (r), which varies based on the underlying structural organization. For a strictly linear arrangement, the number of encountered molecules scales proportionally to r (n=1), whereas for a random two-dimensional (2D) distribution, it follows r^2 (n=2). Intermediate cases, such as fibrillar structures with varying degrees of branching or crossing, exhibit scaling exponents in the 1<n<2 range, reflecting deviations from both purely linear and purely random 2D distributions. By quantifying this scaling exponent, we can infer the degree of molecular organization and identify fibrillar arrangements within the dataset.

<u>References</u>

1. Oliveira, I. A., Freire-de-Lima, L., Penha, L. L., Dias, W. B. & Todeschini, A. R. Trypanosoma cruzi Trans-Sialidase: Structural Features and Biological Implications. in *Proteins and Proteomics of Leishmania and Trypanosoma* (eds Santos, A. L. S., Branquinha, M. H., d'Avila-Levy, C. M., Kneipp, L. F. & Sodré, C. L.) vol. 74 181–201 (Springer Netherlands, Dordrecht, 2014).

2. Pereira-Chioccola, V. L. *et al.* Mucin-like molecules form a negatively charged coat that protects Trypanosoma cruzitrypomastigotes from killing by human anti-α-galactosyl antibodies. *J. Cell Sci.* **113**, 1299–1307 (2000).

3. Tomlinson, S., Pontes De Carvalho, L. C., Vandekerckhove, F. & Nussenzweig, V. Role of sialic acid in the resistance of Trypanosoma cruzi trypomastigotes to complement. *J. Immunol.* **153**, 3141–3147 (1994).

4. De Pablos, L. M. & Osuna, A. Multigene Families in Trypanosoma cruzi and Their Role in Infectivity. *Infect. Immun.* **80**, 2258–2264 (2012).

5. Frevert, U., Schenkman, S. & Nussenzweig, V. Stage-specific expression and intracellular shedding of the cell surface trans-sialidase of Trypanosoma cruzi. *Infect. Immun.* **60**, 2349–2360 (1992).

6. Muia, R. P. *et al.* Identification of glycoproteins targeted by Trypanosoma cruzi trans-sialidase, a virulence factor that disturbs lymphocyte glycosylation. *Glycobiology* **20**, 833–842 (2010).

7. Eugenia Giorgi, M. & De Lederkremer, R. M. Trans-sialidase and mucins of Trypanosoma cruzi: an important interplay for the parasite. *Carbohydr. Res.* **346**, 1389–1393 (2011).

8. Schenkman, S. *et al.* Mucin-like glycoproteins linked to the membrane by glycosylphosphatidylinositol anchor are the major acceptors of sialic acid in a reaction catalyzed by trans-sialidase in metacyclic forms of Trypanosoma cruzi. *Mol. Biochem. Parasitol.* **59**, 293–303 (1993).

9. Almeida, I. C., Ferguson, M. A., Schenkman, S. & Travassos, L. R. Lytic anti- *α* -galactosyl antibodies from patients with chronic Chagas' disease recognize novel *O* -linked oligosaccharides on mucin-like glycosyl-phosphatidylinositol-anchored glycoproteins of *Trypanosoma cruzi*. *Biochem. J.* **304**, 793–802 (1994).

10. Freitas, L. M. *et al.* Genomic Analyses, Gene Expression and Antigenic Profile of the Trans-Sialidase Superfamily of Trypanosoma cruzi Reveal an Undetected Level of Complexity. *PLoS ONE* **6**, e25914 (2011).

11. Di Noia, J. M., Buscaglia, C. A., De Marchi, C. R., Almeida, I. C. & Frasch, A. C. C. A Trypanosoma cruzi small surface molecule provides the first immunological evidence that Chagas' disease is due to a single parasite lineage. *J. Exp. Med.* **195**, 401–413 (2002).

12. Buscaglia, C. A., Campo, V. A., Frasch, A. C. C. & Di Noia, J. M. Trypanosoma cruzi surface mucins: host-dependent coat diversity. *Nat. Rev. Microbiol.* **4**, 229–236 (2006).

13. Campetella, O., Buscaglia, C. A., Mucci, J. & Leguizamón, M. S. Parasite-host glycan interactions during Trypanosoma cruzi infection: trans-Sialidase rides the show. *Biochim. Biophys. Acta BBA - Mol. Basis Dis.* **1866**, 165692 (2020).

14. Lantos, A. B. *et al.* Sialic Acid Glycobiology Unveils Trypanosoma cruzi Trypomastigote Membrane Physiology. *PLOS Pathog.* **12**, e1005559 (2016).

15. Mucci, J., Lantos, A. B., Buscaglia, C. A., Leguizamón, M. S. & Campetella, O. The Trypanosoma cruzi Surface, a Nanoscale Patchwork Quilt. *Trends Parasitol.* **33**, 102–112 (2017).

16. Paladino, S. *et al.* Protein oligomerization modulates raft partitioning and apical sorting of GPI-anchored proteins. *J. Cell Biol.* **167**, 699–709 (2004).

17. Benting, J. H., Rietveld, A. G. & Simons, K. N-Glycans Mediate the Apical Sorting of a Gpi-Anchored, Raft-Associated Protein in Madin-Darby Canine Kidney Cells. *J. Cell Biol.* **146**, 313–320 (1999).

18. Maeda, Y. *et al.* Fatty Acid Remodeling of GPI-anchored Proteins Is Required for Their Raft Association. *Mol. Biol. Cell* **18**, 1497–1506 (2007).

19. Miyagawa-Yamaguchi, A., Kotani, N. & Honke, K. Each GPI-anchored protein species forms a specific lipid raft depending on its GPI attachment signal. *Glycoconj. J.* **32**, 531–540 (2015).

20. Rust, M. J., Bates, M. & Zhuang, X. Sub-diffraction-limit imaging by stochastic optical reconstruction microscopy (STORM). *Nat. Methods* **3**, 793–796 (2006).

21. Heilemann, M. *et al.* Subdiffraction-Resolution Fluorescence Imaging with Conventional Fluorescent Probes. *Angew. Chem. Int. Ed.* **47**, 6172–6176 (2008).

22. Buscaglia, C. A., Campetella, O., Leguizamón, M. S. & Frasch, A. C. C. The Repetitive Domain of *Trypanosoma cruzi trans* -Sialidase Enhances the Immune Response against the Catalytic Domain. *J. Infect. Dis.* **177**, 431–436 (1998).

23. Prescher, J. A. & Bertozzi, C. R. Chemistry in living systems. *Nat. Chem. Biol.* **1**, 13–21 (2005).

24. Ester, M., Kriegel, H.-P., Sander, J. & Xu, X. *A Density-Based Algorithm for Discovering Clusters in Large Spatial Databases with Noise*. 226–331 (1996).

25. Moulavi, D., Jaskowiak, P. A., Campello, R. J. G. B., Zimek, A. & Sander, J. Density-Based Clustering Validation. in *Proceedings of the 2014 SIAM International Conference on Data Mining* 839–847 (Society for Industrial and Applied Mathematics, 2014). doi:10.1137/1.9781611973440.96.

26. Lillemeier, B. F. *et al.* TCR and Lat are expressed on separate protein islands on T cell membranes and concatenate during activation. *Nat. Immunol.* **11**, 90–96 (2010).

27. Pike, L. J. Rafts defined: a report on the Keystone symposium on lipid rafts and cell function. *J. Lipid Res.* **47**, 1597–1598 (2006).
28. Whelan, D. R. & Bell, T. D. M. Image artifacts in Single Molecule Localization Microscopy: why optimization of sample preparation protocols matters. *Sci. Rep.* **5**, 7924 (2015).
29. Irgen-Gioro, S., Yoshida, S., Walling, V. & Chong, S. Fixation can change the appearance of phase separation in living cells. *eLife* **11**, e79903 (2022).
30. Ichikawa, T. *et al.* Chemical fixation creates nanoscale clusters on the cell surface by aggregating membrane proteins. *Commun. Biol.* **5**, 487 (2022).
31. Yoshida, S. R., Maity, B. K. & Chong, S. Visualizing Protein Localizations in Fixed Cells: Caveats and the Underlying Mechanisms. *J. Phys. Chem. B* **127**, 4165–4173 (2023).
32. Dempsey, G. T., Vaughan, J. C., Chen, K. H., Bates, M. & Zhuang, X. Evaluation of fluorophores for optimal performance in localization-based super-resolution imaging. *Nat. Methods* **8**, 1027–1036 (2011).
33. Szalai, A. M., Lopez, L. F., Morales-Vásquez, M. Á., Stefani, F. D. & Aramendía, P. F. Analysis of sparse molecular distributions in fibrous arrangements based on the distance to the first neighbor in single molecule localization microscopy. *Nanoscale* **12**, 9495–9506 (2020).
34. Yu, H. *et al.* A Multifunctional *Pasteurella multocida* Sialyltransferase: A Powerful Tool for the Synthesis of Sialoside Libraries. *J. Am. Chem. Soc.* **127**, 17618–17619 (2005).
35. Schnitzbauer, J., Strauss, M. T., Schlichthaerle, T., Schueder, F. & Jungmann, R. Super-resolution microscopy with DNA-PAINT. *Nat. Protoc.* **12**, 1198–1228 (2017).
36. Smith, C. S., Joseph, N., Rieger, B. & Lidke, K. A. Fast, single-molecule localization that achieves theoretically minimum uncertainty. *Nat. Methods* **7**, 373–375 (2010).
37. Endesfelder, U., Malkusch, S., Fricke, F. & Heilemann, M. A simple method to estimate the average localization precision of a single-molecule localization microscopy experiment. *Histochem. Cell Biol.* **141**, 629–638 (2014).

Acknowledgements

F.D.S. and A.M.S. acknowledge the Alexander von Humboldt Foundation. F.D.S thanks Exemys S.R.L. for support with the hardware. J.M. thanks Liliana Sferco and Agustina Chidichimo for help with parasite cultures and Francisco Güaimas for advice on microscopy. We are grateful to Dr. Esteban Erben (IIB-UNSAM, Buenos Aires) for providing *T. brucei* parasite and anti-VSG 221 antibody.

Author contributions

G.E. performed super-resolution imaging measurements, developed code for the data analysis and analyzed the data and prepared the figures. R.P.P. and M.M.C. prepared the *T. cruzi* samples and performed the biochemical assays. L.F.L performed super-resolution imaging. L.F.L. and A.M.S conceived analysis with G.E.. L.A.M. performed preliminary super-resolution measurements. F.D.S, O.E.C and J.M. conceived the project and designed the experiments. G.E., F.D.S., L.F.L and J.M wrote the manuscript with input from all authors. F.D.S and J.M. supervised the project.

Funding

This work was funded by Consejo Nacional de Investigaciones Científicas y Técnicas (CONICET, Argentina), and through grants from the Agencia Nacional de Promoción de la Investigación, el Desarrollo Tecnológico y la Innovación (ANPCyT, Argentina, PICT V 2014-3729, PICT-2017-0870 and PICT-2021-01216) and the National Institute of Allergy and Infectious Diseases (NIAID) of the National Institutes of Health under awards number R01AI104531 (to OC) and R01AI191327 (to JM). The funders had no role in the design of studies, data collection, and analysis, or in the decision to publish or the preparation of the manuscript.

Data availability statement

All data included in this work along with the open-source code used to analyze the data and generate the figures are publicly available in https://zenodo.org/records/16325107